

Dynamics of nascent current filaments in low-temperature impurity breakdown

M. Gaa, R. E. Kunz, and E. Schöll

Institut für Theoretische Physik, Technische Universität Berlin, Hardenbergstraße 36, D-10623 Berlin, Germany

(Received 11 October 1995)

We present two-dimensional simulations showing the spatiotemporal dynamics of the formation of current filaments in n -type GaAs films in the regime of impurity impact ionization breakdown. From the spatial distribution of carrier densities, electron temperature, current density, and electric field for nascent and for fully developed filaments, we find a three-stage scenario for breakdown: (i) front creation and propagation from the cathode, (ii) stagnation in the phase of a rudimentary filament, (iii) filament growth. Our model combines semiclassical rate equations with microscopic transport parameters, which are obtained from Monte Carlo simulations. [S0163-1829(96)04823-0]

I. INTRODUCTION

Impact ionization of impurities in doped semiconductors at low temperature leads to a sharp increase of the carrier density, and hence the conductivity, if a sufficiently large electric field is applied. Depending on the precise nature of the underlying generation-recombination (GR) kinetics, strongly nonlinear current density-field characteristics result, which may be either monotonically increasing or S shaped with a regime of negative differential conductivity.¹ In this regime, a variety of spatiotemporal instabilities may occur.² Self-organized transitions of a spatially homogeneous low-conductivity state to a high-conductivity state characterized by inhomogeneous, filamentary current flow are prominent examples. While the stationary structure and the possible nonlinear dynamic and chaotic oscillatory behavior of these current filaments has been widely investigated, both experimentally³⁻⁶ and theoretically⁷⁻¹³ in a variety of semiconducting materials, e.g., p -type Ge or n -type GaAs at liquid helium temperatures, little is known about the spatiotemporal dynamics of their formation process.

As actual measurement techniques are either space or time resolved, investigations concentrate on fully developed filaments as stationary or oscillating structures; hence there is almost no experimental information available on how current filaments arise. Previous theoretical attempts to model current filaments were confined to one-dimensional (1D) simulations, where only the transverse spatial coordinate perpendicular to the current flow was taken into account.⁷⁻¹² The dipolar electric field between two point contacts was included in a recent phenomenological model for current filaments in n -type GaAs, but the calculations were effectively reduced to one (transverse) dimension by several simplifying assumptions.¹³ While there has been recent progress in the microscopic analysis of low-temperature impurity breakdown in terms of single-particle¹⁴ and many-particle Monte Carlo (MC) simulations¹⁵ for p -type Ge and for n -type GaAs,^{16,17} the spatiotemporal modes of the breakdown process have so far merely been investigated in a one-dimensional longitudinal model for p -type Ge, a model that neglects the transverse spatial degree of freedom and, therefore, cannot explain filamentation.¹⁸ In order to study the nascent of current filaments, it is necessary to combine the

transverse and the longitudinal degrees of freedom for a realistic two-dimensional sample geometry with appropriately modeled contacts, and include detailed microscopic information on the GR kinetics as obtained from MC simulations. This is the aim of the present paper.

Because of the complexity of the resulting system of coupled nonlinear partial differential equations, it is no longer feasible to use the particle-in-cell algorithm of Refs. 9,10 for the transverse nonlinear and chaotic dynamics of current filaments in p -type Ge, which uses an explicit Euler scheme to propagate a solution forward in time. Rather, we must develop an efficient implicit simulation algorithm to guarantee the stability of the solutions in time. Some preliminary results have been presented recently.¹⁹ Here, we demonstrate the mechanism responsible for the formation of current filaments in semiconductors when a voltage larger than a threshold is applied, and compute the current-voltage characteristic of the stationary filamentary branch for n -type GaAs. The paper is organized as follows. In Sec. II, we present the set of partial differential equations governing the dynamics of current filament formation, and show how the GR rates are derived from MC simulations. The main results of the simulation of the current filament formation are presented and discussed in Sec. III. For a two-dimensional sample geometry with point contacts, we compute in Sec. IV the fully developed current filaments constituting the highly conducting branch of the S -shaped current-voltage characteristic and compare it with the states on the low conducting branch. In Sec. V, we draw some conclusions.

II. MODEL

A. Constitutive equations

We consider a doped semiconductor at helium temperatures. In the following, we shall assume n -type material; p -type semiconductors can be treated analogously. The carrier density in the conduction band, and hence the current density, is determined by the GR processes of carriers between the conduction band and the donor levels. The experimentally observed S -shaped current density-field relation in the regime of impurity breakdown can be explained in terms of standard GR kinetics, only if impact ionization from at least two impurity levels is taken into account.^{20,21} There-

fore, we model the infinite hydrogenlike energy spectrum of the shallow donors by the ground state and an “effective” excited state close to the band edge. In this case, the state of the system can be characterized by the spatial distribution of the carrier densities in the conduction band $n(\mathbf{x}, t)$, as well as in the impurity ground state and excited state $n_1(\mathbf{x}, t)$, $n_2(\mathbf{x}, t)$, respectively, where \mathbf{x} is the spatial coordinate and t denotes time.

The temporal evolution of n is then governed by the continuity equation,

$$\dot{n} = \frac{1}{e} \nabla \cdot \mathbf{j} + \phi(n, n_1, n_2, |\mathcal{E}|), \quad (1)$$

where the dot denotes the partial derivative with respect to time, e is the electron charge, and \mathcal{E} is the local electric field within the sample. Within the drift-diffusion approximation the current density \mathbf{j} can be expressed as

$$\mathbf{j} = e(n\mu\mathcal{E} + D\nabla n), \quad (2)$$

with the diffusion constant D and the mobility μ . We assume the validity of the Einstein relation $D = \mu k_B T_L / e$, where k_B is Boltzmann’s constant and T_L is the lattice temperature.

The rate ϕ of GR processes depends on the local values of the carrier densities in the conduction band and at the impurities, given by n , n_1 , and n_2 , respectively, and the strength of the electric field $\mathcal{E} = |\mathcal{E}|$. Analogously, rates ϕ_1 , ϕ_2 determining the temporal evolution of n_1 , n_2 can be defined as

$$\dot{n}_i = \phi_i(n, n_1, n_2, \mathcal{E}), \quad (3)$$

with $i = 1, 2$.

In an explicit model⁷ for n -type GaAs at 4.2 K, the GR rates are given by

$$\phi = X_1^s n_2 - T_1^s n p_t + X_1 n n_1 + X_1^* n n_2, \quad (4)$$

$$\phi_1 = T^* n_2 - X^* n_1 - X_1 n n_1, \quad (5)$$

$$\phi_2 = -\phi - \phi_1, \quad (6)$$

where $p_t = N_D - n_1 - n_2$ is the density of ionized donors, N_D is the total density of donors, X_1^s is the thermal ionization coefficient of the excited level, T_1^s is its capture coefficient, X_1 , X_1^* are the impact ionization coefficients from the ground and excited level, respectively, X^* , T^* denote the transition coefficients from the ground level to the excited level and vice versa, respectively.

The electric field is coupled to the carrier densities via Poisson’s equation,

$$\epsilon \nabla \cdot \mathcal{E} = e(N_D^* - n_1 - n_2 - n), \quad (7)$$

where ϵ is the dielectric constant and $N_D^* \equiv N_D - N_A$ holds with the compensating acceptor concentration N_A . From equations (1),(3),(6),(7), the charge conservation equation can be derived, given by

$$\nabla \cdot \mathbf{J} = 0, \quad (8)$$

with $\mathbf{J} = \epsilon \dot{\mathcal{E}} + \mathbf{j}$, where \mathbf{J} is the total current density composed of displacement current and conduction current densities. If the initial values of n , n_1 , n_2 , and \mathcal{E} satisfy Poisson’s equation (7), (7) and (8) are not independent and we can substitute (7) by (8) for the numerical treatment of the time-dependent problem in the drift-diffusion approximation. In many cases, this approach turns out to be advantageous.^{22–24}

B. Generation-recombination coefficients

The essential nonlinearities of the constitutive model equations (1)–(8) in the regime of low-temperature impurity breakdown are contained in the dependence of the GR coefficients upon n , n_1 , n_2 , and \mathcal{E} . In order to derive these from a microscopic theory, we have performed single-particle MC simulations for a spatially homogeneous steady state as described in Ref. 16. Thermal ionization of the excited donor level, acoustic phonon-assisted recombination into the excited level (Lax-Abakumov),^{25,26} and impact ionization from both the ground and the excited donor level were included as band-impurity processes. The relevant intraband scattering processes were elastic ionized impurity scattering (Conwell-Weisskopf approximation) and inelastic acoustic deformation potential scattering. (Optical phonon scattering is neglected because of the low lattice temperature, although optical phonon emission becomes relevant for energies above 36 meV.²⁷ However, those states are not frequently populated except at highest fields.¹⁷)

The microscopic rates of all band-impurity processes depend upon the carrier densities in the band and impurity states, which in turn depend upon the nonequilibrium carrier distribution function. To obtain these carrier densities, the MC method has to be combined self-consistently with the rate equations (1)–(3) in the homogeneous steady state, where the GR coefficients X_1 , X_1^* , T_1^s are calculated by averaging the microscopic transition probabilities (P_{ii}^1 , P_{ii}^2 , P_{rec} for impact ionization from the ground state, the excited state, and capture, respectively) over the nonequilibrium distribution function $f(\mathbf{k})$, which is extracted from the MC simulation at each step:

$$\begin{aligned} X_1(n, n_1, n_2, \mathcal{E}) &= \frac{1}{nn_1} \int d^3k f(\mathbf{k}; n, n_1, n_2, \mathcal{E}) P_{ii}^1(\mathbf{k}, n_1), \\ X_1^*(n, n_1, n_2, \mathcal{E}) &= \frac{1}{nn_2} \int d^3k f(\mathbf{k}; n, n_1, n_2, \mathcal{E}) P_{ii}^2(\mathbf{k}, n_2), \end{aligned} \quad (9)$$

$$T_1^s(n, n_1, n_2, \mathcal{E}) = \frac{1}{np_t} \int d^3k f(\mathbf{k}; n, n_1, n_2, \mathcal{E}) P_{\text{rec}}(\mathbf{k}, p_t).$$

Note that f , and hence X_1 , X_1^* , and T_1^s , in turn depend parametrically on n , n_1 , n_2 , and \mathcal{E} . An iteration procedure, where n_1 and n_2 are expressed by their steady-state dependence on n and \mathcal{E} , is used to solve the above problem self-consistently.¹⁶

As a result, the impact ionization coefficients X_1 and X_1^* as well as the capture coefficient T_1^s depend not only on the local electric field \mathcal{E} , but also on the electron concentration n . This dependence on n is associated with a higher electron temperature T_e^{up} on the upper branch of the S shaped $n(\mathcal{E})$

TABLE I. Generation-recombination parameters from a fit to Monte Carlo data for n -type GaAs at 4.2 K.

i	a_i	b_i	c_i	d_i	e_i	g_i
1	2.366	3.417	1.161×10^{-5}	7.530×10^{-3}	4.979×10^{-6}	6.138×10^{-3}
2	18.111	1.689	6.687	0.458	9.726	-0.265
3	2.896	6.098	5.928	4.657	-0.278	1.254
4	1.405×10^2	6.789×10^2	0.694	1.030		
5	57.967	63.191	6.104×10^{-2}	2.836×10^{-2}		

characteristic as compared to the values T_e^{10} on the lower and the middle branch as shown in Ref. 19. The MC data for the electron temperature can be represented by smooth fit functions

$$T_e^{\text{up}}(\mathcal{E}) = a_1 + \frac{a_2}{1 + \exp(a_3 - a_4 \gamma_2 \mathcal{E})} + a_5 \gamma_2 \mathcal{E}, \quad (10a)$$

$$T_e^{10}(\mathcal{E}) = b_1 + \frac{b_2}{1 + \exp(b_3 - b_4 \gamma_2 \mathcal{E})} + b_5 \gamma_2 \mathcal{E}, \quad (10b)$$

with parameters a_i, b_i ($i=1, \dots, 5$) as given in Table I. A strong increase of T_e with rising electric field occurs on the high-conductivity branch as opposed to only a slight increase on the low-conductivity branch. Physically, the strong increase is associated with a population inversion between the donor ground and excited state on the upper branch. For $\mathcal{E} > 9$ V/cm, impact ionization does no longer contribute to energy relaxation in a significant way, since the donor ground states are almost completely ionized and impact ionization from the excited state dominates, which is now more strongly populated than the ground state. Because of the much smaller energies involved, this process cools less efficiently. The transition from T_e^{10} to T_e^{up} at a certain threshold electron density n_{th} corresponding to the smallest value of n on the upper branch may be described by a hyperbolic tangent. Thus, the MC data for the electron temperature in dependence on \mathcal{E} and n can be parametrized by the following smooth fit function:

$$T_e(\mathcal{E}, n) = \frac{1}{2} \gamma_0^{-1} \{ [T_e^{\text{up}}(\mathcal{E}) + T_e^{10}(\mathcal{E})] + [T_e^{\text{up}}(\mathcal{E}) - T_e^{10}(\mathcal{E})] \tanh[\log_{10}(\gamma_1 n / n_{\text{th}})] \}. \quad (10c)$$

It is possible to express the dependence of the GR coefficients upon \mathcal{E} and n through the electron temperature $T_e(\mathcal{E}, n)$, as shown in Ref. 19. The MC data for impact ionization from the ground state and the excited state can be represented by the fit functions,

$$X_1(T_e) = \gamma_3 c_1 \exp \left[\frac{c_2}{1 + \exp(c_3 - c_4 \gamma_0 T_e)} + c_5 \gamma_0 T_e \right], \quad (11a)$$

$$X_1^*(T_e) = \gamma_3 d_1 \exp \left[\frac{d_2}{1 + \exp(d_3 - d_4 \gamma_0 T_e)} + d_5 \gamma_0 T_e \right]. \quad (11b)$$

X_1 exhibits a sharp increase between 30 and 50 K, while X_1^* shows a much weaker dependence on T_e , because of the much smaller ionization energy. The capture coefficient is represented by

$$T_1^s(T_e, n) = \frac{1}{2} \gamma_3 \{ [T_1^{\text{sup}}(T_e) + T_1^{s10}(T_e)] + [T_1^{\text{sup}}(T_e) - T_1^{s10}(T_e)] \tanh[\log_{10}(\gamma_1 n / n_{\text{th}})] \}, \quad (11c)$$

$$T_1^{\text{sup}}(T_e) = e_1 \exp[e_2(\gamma_0 T_e - q_1)e^{\epsilon_3}], \quad (11d)$$

$$T_1^{s10}(T_e) = g_1 \exp[g_2(\gamma_0 T_e)^{g_3}], \quad (11e)$$

where different functions $T_1^{\text{sup}}(T_e)$ and $T_1^{s10}(T_e)$ have been used to express the enhancement of T_1^s at the onset of the upper branch of the $n(\mathcal{E})$ characteristic. The enhancement occurs due to strong impact ionization, which scatters many carriers back to the band minimum, from where they can recombine with high probability. Generally, the capture rate decreases with increasing carrier temperature, due to the reduced Coulombic scattering cross section at higher carrier energy. The parameters $a_i, b_i, c_i, d_i, e_j, g_j$, $i=1, \dots, 5$, $j=1, 2, 3$, are results from a nonlinear fit with fixed parameters n_{th} and q_1 . The factors $\gamma_0, \gamma_1, \gamma_2, \gamma_3$ are ‘‘scaling’’ factors that are used to attach the correct units to the equations.

In the following, our strategy will be to insert the fitted analytical representations of the MC data into the macroscopic equations (1)–(8). We use this approach in order to take into account as much detailed information as possible about the microscopic scattering processes, while still retaining manageable expressions. As a check of consistency, the spatially uniform stationary $n(\mathcal{E})$ characteristic obtained with the fit functions from (4)–(6) in the steady state using the condition of charge neutrality $N_D^* = n(\mathcal{E}) + n_1(\mathcal{E}, n) + n_2(\mathcal{E}, n)$, can be compared with the characteristic obtained by direct MC simulation as done in Ref. 19. The successful reproduction of the **S** shape of $n(\mathcal{E})$ justifies the arbitrary choice of basis functions for the fit of X_1, X_1^*, T_1^s , and T_e . The construction of these functions takes into account that the MC data for $T_e(\mathcal{E}, n)$ and for $T_1^s(T_e, n)$ take on dif-

ferent values for the middle and the lower branch of the characteristic on the one hand and the upper branch on the other. If $n \ll n_{\text{th}} N_D^*$ holds, only the lower and middle branch of the “S” dominates; however, for $n \gg n_{\text{th}} N_D^*$ the upper branch prevails. All numerical parameters of the GR rates are given in Table I.

C. Numerical simulation

In order to solve the space- and time-dependent constitutive equations (1)–(6),(8) for a 2D sample geometry under voltage control, we use an implicit finite element scheme.^{24,28} Due to the strong nonlinearities and steep spatial gradients in the regime of impurity breakdown, an elaborate numerical algorithm with efficient time step control and update of the spatial grid is required. Our algorithm is not based on an explicit Euler scheme as the particle-in-cell algorithms of Refs. 9,10, but uses a semi-implicit scheme for the propagation of the solutions of (1)–(6),(8) in time. This guarantees a degree of numerical stability of the solutions of these highly complex nonlinear spatiotemporal partial differential equations, which an explicit Euler scheme could not provide without using unreasonably small iteration time steps and hence requiring amounts of CPU time that would make it unfeasible to use simulations as an investigative tool of studying filament formation in 2D.

We choose a square sample geometry with side lengths $L_x = L_z = 0.02$ cm representing a thin GaAs film. The thickness of the film is $L_y = 1.4 \times 10^{-3}$ cm. This value is only relevant for the scaling of the integral current through the sample. We model point contacts by applying Dirichlet boundary conditions to two opposite regions of length $L_c = 8 \times 10^{-4}$ cm at the centers of the sample edges parallel to the z axis. At the contacts n is fixed to a value $n_D = 5 \times 10^{15}$ cm⁻³ to model Ohmic contacts. All other

TABLE II. Material parameters for n -type GaAs.

Parameter	Symbol	Value
Donor concentration	N_D	7.0×10^{15} cm ⁻³
Acceptor concentration	N_A	2.0×10^{15} cm ⁻³
Lattice temperature	T_L	4.2 K
Mobility	μ	1.0×10^5 cm ² /Vs
Dielectric constant	ϵ	$10.9 \epsilon_0$
Dielectric relaxation time	τ_M	7.83×10^{-14} s

boundaries are treated as insulating where the components of the current density \mathbf{j} and the electric field \mathcal{E} perpendicular to the boundaries vanish. We start our simulation at time $t_0 \equiv 0$ with the sample in thermal and chemical equilibrium, i.e., vanishing currents and fluxes. The material parameters for the n -type GaAs sample are given in Table II.

III. FILAMENT FORMATION

In this section, we study the nascence of current filaments when the applied voltage is switched rapidly to a value above breakdown threshold, so that the semiconductor is forced from the nearly insulating state to a highly conducting state. Within 1ps the voltage is linearly increased from $U=0$ V to $U=0.48$ V, corresponding to an average field of $\mathcal{E}=24$ V/cm. Due to the Ohmic nature of the contacts, we find small regions in the vicinity of the contacts in which the electron concentration n in the conduction band is largely enhanced compared to the bulk where it is very low.¹⁹ Practically all carriers are bound in the donor ground state. The carrier concentration in the excited donor level n_2 [Fig. 1(a)] and the current density $\mathbf{j} \equiv |j|$ [Fig. 2(a)] are very low and remain so during the voltage increase. The electron temperature in the whole sample is equal to the lattice temperature

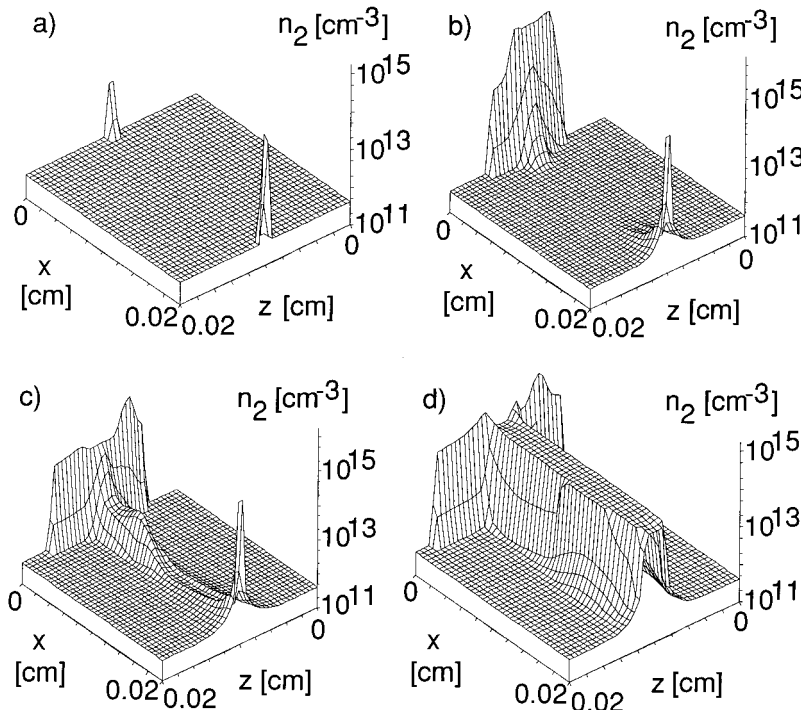


FIG. 1. Temporal evolution of the electron density $n_2(x,z)$ in the excited donor level as a function of the spatial coordinates x and z for a square sample with two point contacts. (a) $t=1$ ps, (b) $t=0.5$ ns, (c) $t=1.0$ ns, (d) $t=2.5$ ns. The applied voltage $U=0.48$ V corresponds to an average field $\mathcal{E}=24$ V/cm, i.e., above the threshold field $\mathcal{E}_{\text{th}}=17$ V/cm of the homogeneous $n(\mathcal{E})$ characteristic (calculated with the parameters of Tables I, II).

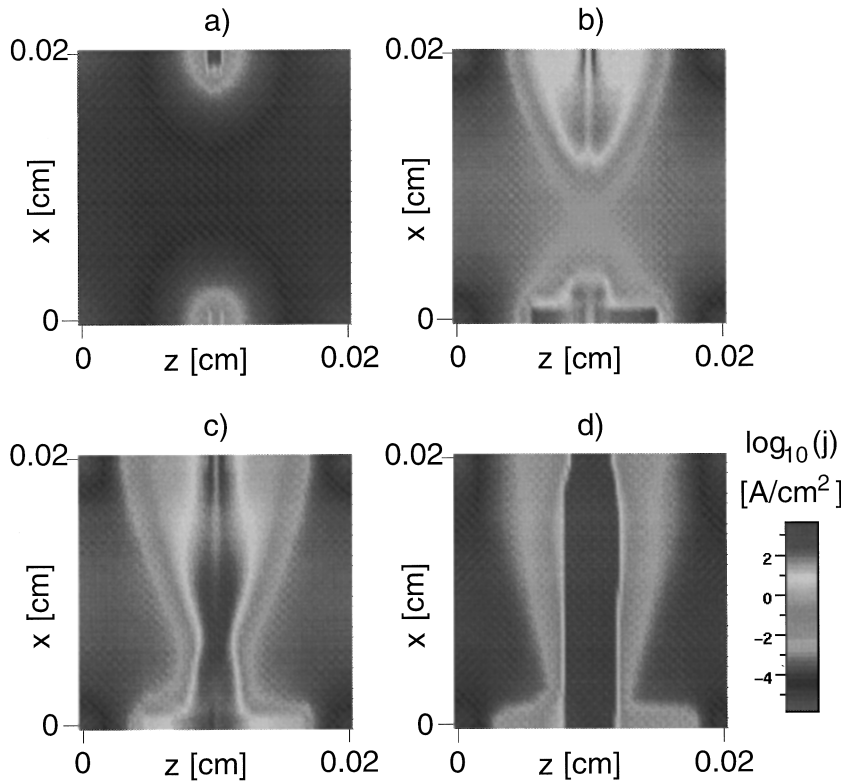


FIG. 2. Temporal evolution of the current density $j(x,z)$. Time steps and voltage as in Fig. 1. The gray scale of the density plots corresponds to a logarithmic scale of j . Note that the injecting cathode is at the top.

T_L (Ref. 19). Due to the assumed voltage control, the electric field \mathcal{E} reacts quasi-instantaneously forming a dipole-like electric field distribution [Figs. 3(a), 4(a)] and inducing enlarged areas of increased electron density at both the cathode and the anode. Subsequently, impact ionization multiplies the electron concentration at the cathode (at $x=0.02$ cm) and establishes a front that moves towards the anode [Figs. 1(b), 2(b)]. The propagation of the front is accompanied by a high field domain [Fig. 3(b)] associated with a slightly increased electron temperature T_e . Although the electric field

behind the front is smaller than in front of it, for reasons of current conservation, the increased electron density in regions passed by the front is almost conserved because recombination is a much slower process than generation. Hence impact ionization downstream is encouraged, whereas further generation upstream is inhibited. When the front meets the region of increased carrier density around the anode, a rudimentary filament is formed, albeit with a carrier density several orders of magnitude lower than that corresponding to completely ionized donor states of density

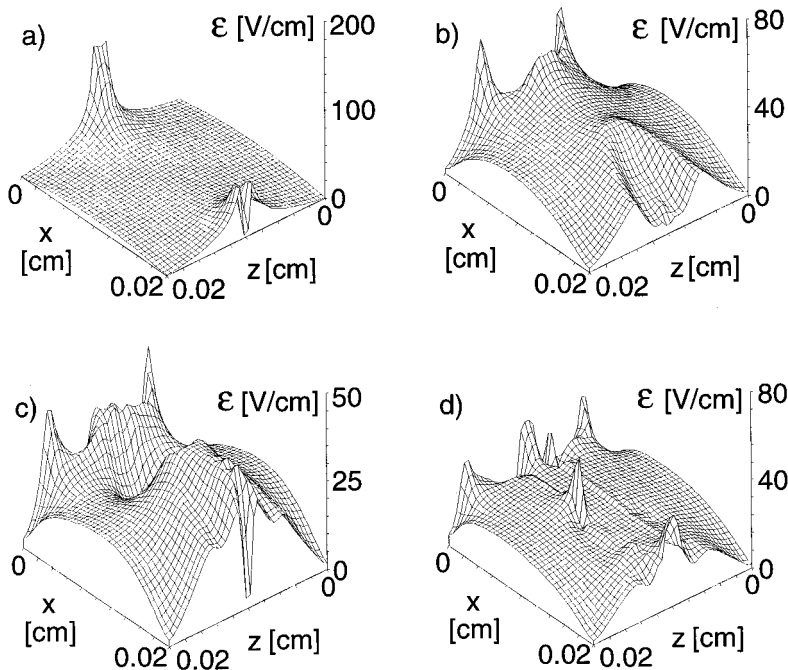


FIG. 3. Temporal evolution of the modulus of the electric field $\mathcal{E}(x,z)$. Time steps and voltage as in Fig. 1.

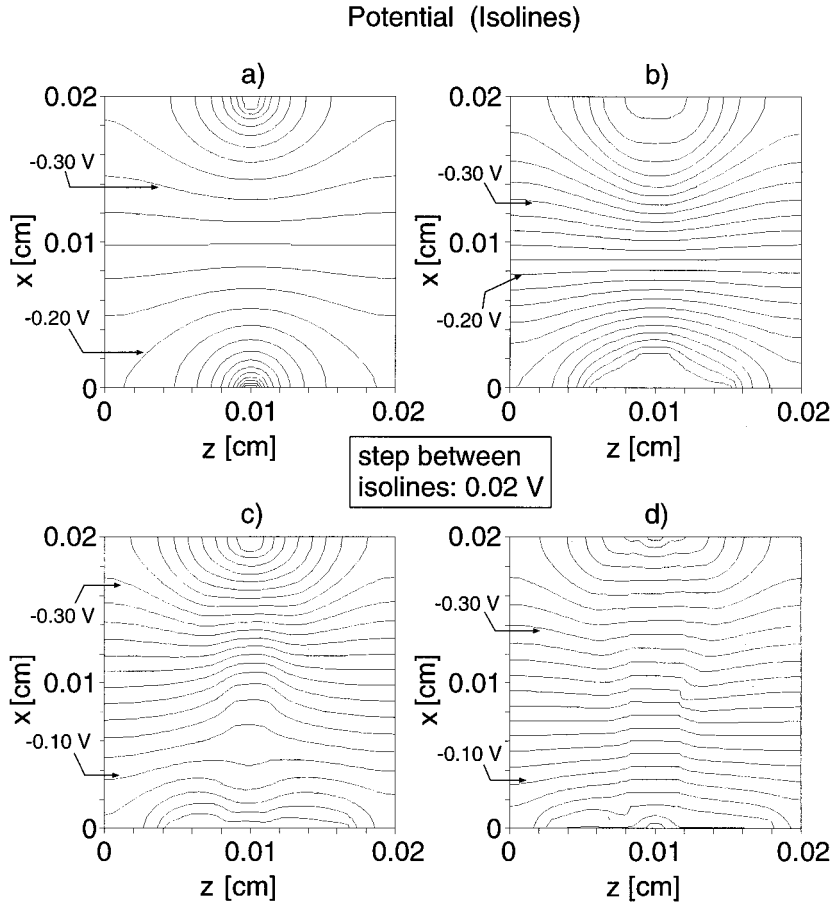


FIG. 4. Temporal evolution of the potential $\Phi(x,z)$. Time steps and voltage as in Fig. 1. Potential isolines are shown.

$N_D^* = 5 \times 10^{15} \text{ cm}^{-3}$. Now donor impact ionization is becoming enhanced in the rudimentary filament, because the excited level n_2 is increasingly populated [Fig. 1(c)]. The current density [Fig. 2(c)] and the electron temperature are significantly growing in the rudimentary filament. The potential distribution Φ is being deformed [Fig. 4(c)] by the nascent filament, and the high field domain reverses its direction of motion and moves back from the anode to the cathode [Fig. 3(c)], again for the reason of current conservation. Finally, impact ionization leads to a uniform increase of electron density until the filament reaches its mature state, where almost all donors are ionized, and the carrier density corresponds to the upper branch of the homogeneous steady state characteristic $n(\mathcal{E})$. Within the filament, the excited donor level is much more highly populated than outside [Fig. 1(d)], nevertheless still only about 2% of the band carriers are trapped in the excited level, while the ground level is *completely* depleted inside the filament. Thus, the population ratio between ground and excited level is inverted in the filament. Also, the current density j and the electron temperature T_e are much larger inside the filament than outside [Fig. 2(d)]. The high field domain vanishes [Fig. 3(d)], and the deformation of the potential distribution is completed [Fig. 4(d)].

During this breakdown process the total current¹⁹ increases rapidly after a stage of very low current [Figs. 1(b)–4(b)], where the front travels from cathode to anode. When the rudimentary filament is established [Figs. 1(c)–4(c)] the current increases, but shows a local minimum in its growth rate. Afterwards the transition to the mature filament [Figs.

1(d)–4(d)] occurs much more rapidly.

Hence, from our simulation, we find three stages of impact ionization breakdown: a stage of front creation and propagation from the injecting contact, i.e., the cathode, (stage I) followed by a stage of stagnation after the front has reached the anode (stage II), and a final stage during which the rudimentary filament grows to a mature filament (stage III). Whereas there are indications from one-dimensional simulations ignoring the transverse z dependence that the stagnation of the breakdown process in the second-stage results from a seesawlike mode, in which a high field domain moves back and forth between the anode and the cathode,¹⁸ the mechanism for the slowing down of the increase in $I(t)$ in the 2D case is not completely clear, but appears to be similar.

IV. FULLY DEVELOPED FILAMENTS

Our simulations in the previous section have shown that the final high-current steady state reached after breakdown is characterized by an inhomogeneous, filamentary current density distribution, as indeed experimentally found by spatially resolved measurements of n -type GaAs at liquid helium temperature.^{5,29,30} We are now in a position to compute the stable parts of the S -shaped stationary current-voltage characteristic from our detailed simulations of the 2D sample.

The procedure to calculate these points is to increase the voltage stepwise and to wait after each step until the system returns to its steady state. We start at zero voltage and increase the voltage until switching from the low conductive

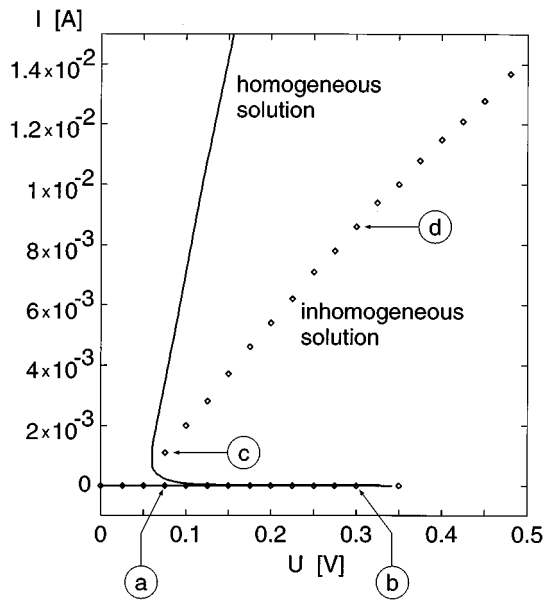


FIG. 5. Stationary current-voltage characteristic calculated with the parameters of Tables I, II, from the spatially inhomogeneous solution of the two-dimensional sample (squares), in comparison with the homogeneous solution (full lines). The letters correspond to the plots shown in Figs. 6–8 below.

state to the highly conductive state occurs, as described in Sec. III. Then, on the upper branch of the characteristic, we let the filament develop completely. Afterwards the voltage is decreased stepwise and again after each step we let the system return to a steady state. This is done until the voltage drops below the holding voltage, where the upper branch becomes unstable and returns to the lower branch. The decision if the system reaches its steady state after increasing the

voltage is based on the information of the total current $I(t)$. When $I(t)$ becomes constant, the steady state is reached.

For this simulation, we use the same initial conditions as described in Sec. II.C. The points on the lower branch are calculated in voltage steps of $\Delta U = 0.025$ V, starting from $U = 0$ V. The voltage increase of ΔU is done linearly within 1 ps. The relaxation time to the steady state turns out to be less than 1 ns. For the calculation of the points on the upper branch, we switch to the highly conductive state at $U = 0.5$ V. Voltage is decreased in steps of $\Delta U = 0.025$ V in the same manner as before.

The resulting points are plotted in Fig. 5, in comparison with the spatially homogeneous steady-state solution. Obviously, on the highly conducting branch, the slope of the homogeneous solution is larger by a factor of about 5 than that of the inhomogeneous solution, whereas on the low conducting branch the current in both cases is almost zero. The reason for the reduced slope is that the current is carried only by the filamentary channel, which has a smaller cross section. Both solutions show an almost constant slope on the highly conducting branch, which is obvious since the carrier density does not change significantly in this regime. The shape of the current-voltage characteristic is in good agreement with characteristics obtained from experiments.³⁰

For four different points on the current-voltage characteristic [labeled (a)–(d) in Fig. 5], we display the spatial distribution of the electron density in the conduction band $n(x, z)$ (Fig. 6) and in the excited donor level $n_2(x, z)$ (Fig. 7), and the potential distribution $\Phi(x, z)$ (Fig. 8). Regarding the electron densities n on the lower branch [Fig. 6(a), (b)], there is just a slight increase in electron concentration in the vicinity of the contacts. With increasing voltage, there is also an increase in the bulk except at the corners of the sample.

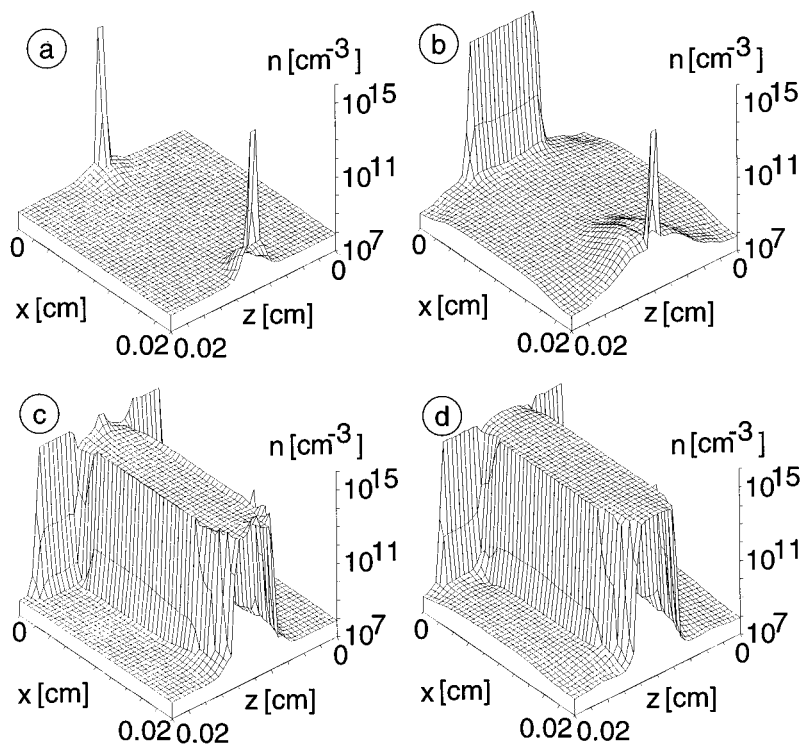


FIG. 6. Electron density $n(x, z)$ in the steady state corresponding to the points labeled (a)–(d) in the current-voltage characteristic of Fig. 5. (a) $U = 0.075$ V (lower branch), (b) $U = 0.3$ V (lower branch), (c) $U = 0.075$ V (upper branch), (d) $U = 0.3$ V (upper branch).

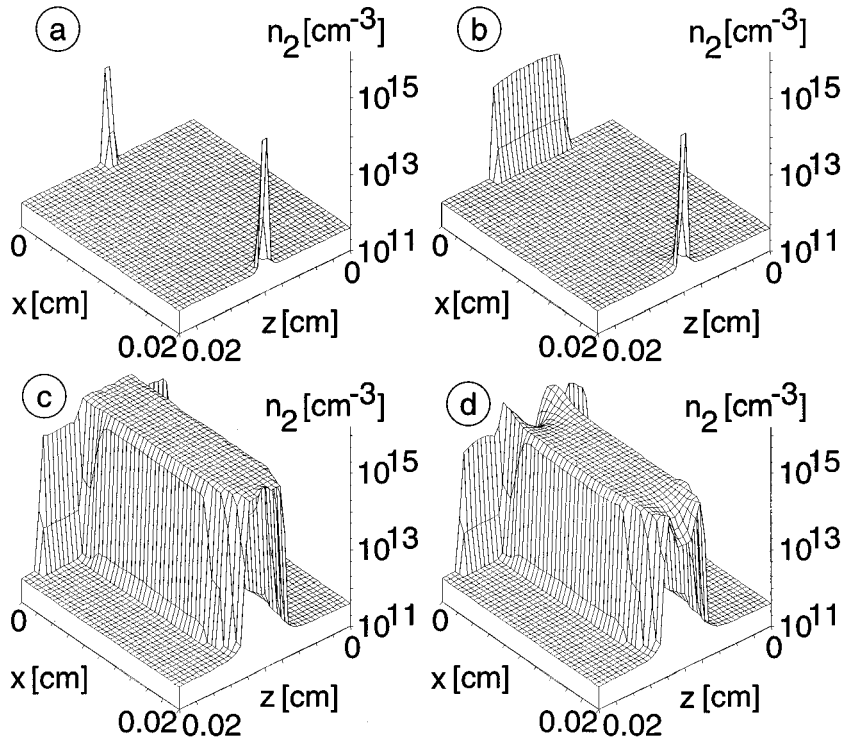


FIG. 7. Same as Fig. 6 for the electron density in the excited donor level $n_2(x, z)$.

On the upper branch [Fig. 6(c),(d)], we have a fully developed filament that shows a slight decrease in electron concentration as the voltage is reduced. For the electron concentration in the excited donor level n_2 , on the lower branch we find just changes in the contact region similar to n . On the

upper branch, however, the concentration n_2 decreases with increasing voltage due to reduced recombination with growing electron temperature.¹⁹ Note that, for the same reason, n_2 assumes its largest values at the filament boundaries and is somewhat smaller in the interior of the filament where the

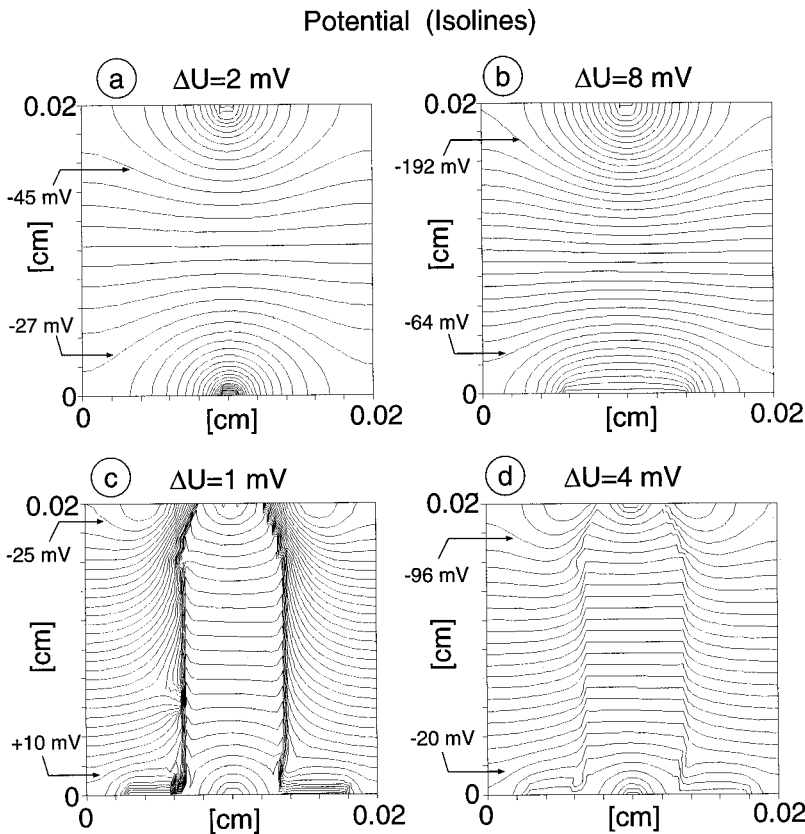


FIG. 8. Same as Fig. 6 for the potential $\Phi(x, z)$. ΔU denotes the steps between the potential isolines shown.

electron temperature is higher. Outside the filament, practically all carriers are trapped in the donor ground level, which is, in turn, strongly depleted inside the filament. Our simulations thus give detailed microscopic information about the density profiles of carriers in band states and in ground and excited donor states in a cross section of the filament. This corrects former phenomenological 1D modeling, which assumed either a peak of n_2 in the filament wall but no population inversion inside the filament,³¹ or monotonic wall profiles of n_2 and n_1 , and values of n much lower than n_1 , n_2 inside the filament.¹³

The potential $\Phi(x, z)$ (Fig. 8) shows a dipolelike distribution for the lower branch and a deformation caused by the filament on the upper branch. There, the electric field is of the same order inside and outside the filament, but distinctly higher at the filament boundaries. All values correspond to the regime of bistability between the holding field and the threshold field of the $n(\mathcal{E})$ characteristic, thus allowing for the spatial coexistence of the low conducting and the highly conducting state.

V. CONCLUSIONS

In this paper, we have presented detailed simulations of the spatiotemporal dynamics of the nascence of a current filament during impurity breakdown. It is shown that this process can be characterized by three stages: (1) front creation at the injecting contact and propagation towards the noninjecting contact, (2) stagnation in the phase of a rudimentary filament when the front has reached the opposite contact, (3) uniform growth of the rudimentary filament to a fully developed filament.

Using our results for the fully developed filaments, we have been able to construct the complete current-voltage characteristic including the highly conducting filamentary

upper branch. Our results are in good agreement with both global $I(U)$ measurements and spatially resolved images of current filaments³² in n -type GaAs obtained from scanning electron microscopy,^{3,29,33} laser scanning microscopy,³⁰ and suppressed photoluminescence measurements.³⁴

Our analysis of the evolution of the spatial distributions of carriers in band and impurity states, of the electron temperature, of the current density, the electric field, and the potential has elucidated the breakdown mechanism and its implications for the formation of current filaments in semiconductors. By combining a self-consistent solution of the carrier continuity equation and Poisson's equation for a two-dimensional sample geometry with single-particle Monte Carlo simulations of the microscopic scattering and generation-recombination processes including impact ionization of shallow impurities, we have developed a powerful tool to study various problems in the field of current instabilities and filamentation. The elaborate numerical algorithm will enable us to consider different sample structures and contact geometries, including multiple arrays of point contacts as proposed recently with the aim of realizing multifilamentary switching.³⁵ Future research will be conducted in this direction.

ACKNOWLEDGMENTS

We wish to thank Professor H. Gajewski and Dr. R. Nürnberg from the Weierstrass-Institut für Angewandte Analysis und Stochastik, Berlin, for their help in adopting our equations to their algorithms. For fruitful discussions, we also thank Professor W. Prettl, Dr. V. Novak, U. Margull, and C. Wimmer from the University of Regensburg and Professor M. Asche and Dr. H. Kostial from the Paul-Drude-Institut, Berlin. Partial support from Deutsche Forschungsgemeinschaft is gratefully acknowledged.

-
- ¹M. P. Shaw, V. V. Mitin, E. Schöll, and H. L. Grubin, *The Physics of Instabilities in Solid State Electron Devices* (Plenum Press, New York, 1992).
- ²*Nonlinear Dynamics and Pattern Formation in Semiconductors and Devices*, edited by F. J. Niedernostheide (Springer, Berlin, 1995).
- ³K. Aoki and T. Kondo, *Phys. Lett. A* **145**, 281 (1991).
- ⁴F.-J. Niedernostheide, B. S. Kerner, and H.-G. Purwins, *Phys. Rev. B* **46**, 7559 (1992).
- ⁵J. Spangler, U. Margull, and W. Prettl, *Phys. Rev. B* **45**, 12 137 (1992).
- ⁶J. Peinke, J. Parisi, O. Rössler, and R. Stoop, *Encounter with Chaos* (Springer, Berlin, Heidelberg, 1992).
- ⁷E. Schöll, *Nonequilibrium Phase Transitions in Semiconductors* (Springer, Berlin, 1987).
- ⁸R. Kunz and E. Schöll, *Z. Phys. B* **89**, 289 (1992).
- ⁹G. Hüpper, K. Pyragas, and E. Schöll, *Phys. Rev. B* **48**, 17 633 (1993).
- ¹⁰G. Hüpper, K. Pyragas, and E. Schöll, *Phys. Rev. B* **47**, 15 515 (1993).
- ¹¹A. Wacker and E. Schöll, *Z. Phys. B* **93**, 431 (1994).
- ¹²B. S. Kerner and V. V. Osipov, *Autosolitons* (Kluwer Academic Publishers, Dordrecht, 1994).
- ¹³V. Novák, C. Wimmer, and W. Prettl, *Phys. Rev. B* **52**, 9023 (1995).
- ¹⁴T. Kuhn, G. Hüpper, W. Quade, A. Rein, E. Schöll, L. Varani, and L. Reggiani, *Phys. Rev. B* **48**, 1478 (1993).
- ¹⁵W. Quade, G. Hüpper, E. Schöll, and T. Kuhn, *Phys. Rev. B* **49**, 13 408 (1994).
- ¹⁶B. Kehrer, W. Quade, and E. Schöll, *Phys. Rev. B* **51**, 7725 (1995).
- ¹⁷H. Kostial, M. Asche, R. Hey, K. Ploog, B. Kehrer, W. Quade, and E. Schöll, *Semicond. Sci. Technol.* **10**, 775 (1995).
- ¹⁸R. E. Kunz and E. Schöll, *Z. Phys. B* **99**, 185 (1996).
- ¹⁹M. Gaa, R. E. Kunz, and E. Schöll, in *Proceedings of the 9th International Conference on Hot Carriers in Semiconductors*, edited by K. Hess, J. P. Leburton, and U. Ravaioli (Plenum, New York, in press).
- ²⁰E. Schöll, *Z. Phys. B* **46**, 23 (1982).
- ²¹A. A. Kastalsky, *Phys. Status Solidi* **15**, 599 (1973).
- ²²S. Selberherr, *Analysis and Simulation of Semiconductor Devices* (Springer, Wien, 1984).
- ²³H. Gajewski, *Z. Angew. Math. Mech.* **2**, 101 (1985).
- ²⁴R. E. Kunz, E. Schöll, R. Nürnberg, and H. Gajewski, *Solid State Electron.* (to be published).

- ²⁵M. Lax, Phys. Rev. **119**, 1502 (1960).
- ²⁶V. N. Abakumov, V. I. Perel, and I. N. Yassievich, Fiz. Tekh. Poluprovodn. **12**, 3 (1978) [Sov. Phys. Semicond. **12**, 1 (1978)].
- ²⁷H. Kostial, Th. Ihn, P. Kleinert, R. Hey, M. Asche, and F. Koch, Phys. Rev. B **47**, 4485 (1993).
- ²⁸R. E. Kunz, *Dynamics of First-Order Phase Transitions* (Harri Deutsch, Frankfurt a.M., 1995).
- ²⁹K. Mayer, R. Gross, J. Parisi, and J. Peinke, Solid State Commun. **63**, 55 (1987).
- ³⁰J. Spangler, B. Finger, C. Wimmer, W. Eberle, and W. Prettl, Semicond. Sci. Technol. **9**, 373 (1994).
- ³¹A. Brandl and W. Prettl, Phys. Rev. Lett. **66**, 3044 (1991).
- ³²U. Rau, K. Aoki, J. Peinke, J. Parisi, W. Clauss, and R. P. Huebener, Z. Phys. B **81**, 53 (1990).
- ³³W. Clauss, U. Rau, J. Peinke, and J. Parisi, J. Appl. Phys. **70**, 232 (1991).
- ³⁴W. Eberle, J. Hirschinger, U. Margull, W. Prettl, V. Novák, and H. Kostial, Appl. Phys. Lett. (to be published).
- ³⁵H. Kostial, K. Ploog, R. Hey, and F. Böbel, J. Appl. Phys. **78**, 4560 (1995).